

Article

Large-Signal Stability Analysis for Islanded DC Microgrids with $n+1$ Parallel Energy-Storage Converters

Xinbo Liu ^{1,*}, Yiran Zhang ¹, Yongbing Suo ², Xiaotong Song ¹ and Jinghua Zhou ¹

¹ School of Electrical and Control Engineering, North China University of Technology, Beijing 100144, China; zhangyiran362@163.com (Y.Z.); songxt@ncut.edu.cn (X.S.); zjh@ncut.edu.cn (J.Z.)

² Beijing Institute of Exploration Engineering, Beijing 100083, China; suoybing@163.com

* Correspondence: liuxinbo@ncut.edu.cn

Abstract: In islanded DC microgrids, the negative impedance characteristics of constant power loads (CPLs) usually introduce instability influences; on the contrary, hybrid energy-storage systems (HESSs) constituted of batteries and supercapacitors (SCs) have stabilization advantages. To guarantee the large-signal stability of islanded DC microgrids with $n+1$ parallel energy-storage converters, an equivalent model is first constructed based on the control strategies of the converters. Then, according to the mixed potential function theory, a large-signal stability criterion, considering powers, inductors, capacitors, the DC bus voltage, the equivalent internal resistances of batteries, the proportional parameters of the inner current loop of n battery DC–DC converters, the proportional parameter of the outer power control loop of the SC DC–DC converter, and the proportional parameter of the inner current loop of the CPLs, is derived. Furthermore, the proposed large-signal stability criterion is optimized via the use of droop control for n battery converters, and coefficients related to the droop coefficients are also taken into account. These involved control parameters reveal the process of regulating the HESS and CPLs instead of ideal modeling and significantly reduce the conservatism of the criterion to some extent. In addition, on the basis of the large-signal stability criterion presented herein, the maximum CPL power that the islanded DC microgrids can stably support is obtained. Finally, simulation and experimental results verify the validity of the provided large-signal-stability criterion. The given procedure of analyzing large-signal stability is more consistent with planning and operating actual DC microgrids.



Citation: Liu, X.; Zhang, Y.; Suo, Y.; Song, X.; Zhou, J. Large-Signal Stability Analysis for Islanded DC Microgrids with $n+1$ Parallel Energy-Storage Converters.

Electronics **2023**, *12*, 4032. <https://doi.org/10.3390/electronics12194032>

Academic Editor: Adel M. Sharaf

Received: 7 August 2023

Revised: 6 September 2023

Accepted: 19 September 2023

Published: 25 September 2023



Copyright: © 2023 by the authors. Licensee MDPI, Basel, Switzerland. This article is an open access article distributed under the terms and conditions of the Creative Commons Attribution (CC BY) license (<https://creativecommons.org/licenses/by/4.0/>).

Keywords: large-signal-stability criteria; islanded DC microgrids; $n+1$ parallel energy-storage converters; mixed potential function

1. Introduction

DC microgrids have emerged as effective solutions for integrating photovoltaic and wind power [1] and connecting energy storage units and DC loads to a DC bus through the use of many converters [2]. Hybrid energy-storage systems (HESSs) constituted of batteries and supercapacitors (SCs) are widely utilized in DC microgrids in order to obtain high energy densities and simultaneously attain high power densities [3–5]. For islanded DC microgrids, large-capacity HESSs are required to provide supplementary power for loads and to absorb extra power from microsources [6,7]. Consequently, many small-capacity batteries cascaded with DC–DC converters are commonly paralleled with each other to achieve a large capacity, and they are also in parallel with SCs and cascaded DC–DC converters. This indicates that a large number of DC–DC converters are in parallel connections in islanded DC microgrids.

Furthermore, closed-loop-controlled loads in DC microgrids are regarded as constant power loads (CPLs) with negative impedance characteristics. The disturbances introduced by power variations from microsources and loads are extremely common in DC microgrids; unfortunately, the positive feedback introduced by CPLs usually magnify these

disturbances and may lead to instability in disturbance-sensitive DC microgrids in island mode [8–11]. Consequently, guaranteeing the large-signal stability of islanded DC microgrids becomes a significant issue.

However, a HESS can sometimes compensate for the dynamic characteristics of CPLs and increase the stability of an islanded DC microgrid to some extent [12,13]. Although control techniques for HESSs and the characteristics of HESSs have gained a significant amount of attention, few studies have derived quantitative design guidelines for HESSs from the aspect of stability enhancement. In particular, many parallel energy-storage DC–DC converters introduce numerous difficulties in investigating large-signal-stability improvements for islanded DC microgrids.

Currently, a great deal of the literature utilizes different methods for analyzing the large-signal stability of DC microgrids [14–19]. In [20–22], a large-signal stability analysis of microgrids was carried out based on the Takagi–Sugeno (TS) fuzzy model. The authors of [21] constructed a TS fuzzy model for AC–DC hybrid microgrids with linear matrix inequalities, and the stability domains were obtained. In [22], a predictive control strategy based on the TS fuzzy model was used to improve the stability margins of DC microgrids. However, the TS fuzzy model method could not derive quantitative stability criteria. In [23,24], the Lyapunov function was adopted to analyze the stability of simple DC microgrids, stability criteria were deduced, and factors affecting the stability were determined simultaneously. Unfortunately, building a Lyapunov function model is very difficult, especially for a complex system.

Then, the mixed potential function method was utilized to model DC microgrids constituting a few converters, sources, and loads, and quantitative large-signal stability criteria were derived [25–29]. The authors of [30] adopted a mixed potential function analysis to propose large-signal-stability criteria in order to guarantee the stability of a DC microgrid. In [31], the effects of CPL power, the DC gain-of-voltage control loop, constant resistance load, and the equivalent internal resistance of the current source were all analyzed to obtain a stability criterion based on a mixed potential function. Furthermore, the authors of [32] considered the regulation parameters of a cascaded converter for CPLs and improved the conservatism of the derived large-signal stability criteria. In [33–36], the mixed potential function was utilized to conduct large-signal stability analyses of DC microgrids containing small-capacity energy-storage systems. However, the current research cannot analyze the large-signal stability of a complex DC microgrid.

At present, large-signal stability analyses of DC microgrids with large-capacity HESSs are rarely carried out because modeling DC microgrids with many parallel energy-storage converters is extremely difficult.

This paper adopts a mixed potential function method to investigate the stability of islanded DC microgrids containing $n+1$ parallel energy-storage converters and derives large-signal stability criteria. The main contributions of the paper are as follows:

- An equivalent model of a complex DC microgrid constituted of microsources, CPLs, batteries, SCs, and $n+1$ parallel energy-storage converters is constructed based on control strategies;
- A large-signal stability criterion is derived by considering the power of the microsource, the power of the CPLs, a time constant, the computational period of the low-pass filter, inductors, capacitors, the DC bus voltage, the battery charging and discharging factor, the equivalent internal resistances of the batteries, the proportional parameters of the inner current loop of the n battery DC–DC converters, the proportional parameter of the outer power control loop of the SC DC–DC converter, and the proportional parameter of the inner current loop of the CPLs;
- The proposed large-signal stability criterion is optimized via the use of droop control for the battery converters, and coefficients related to the droop coefficients are taken into account. The maximum CPL power that islanded DC microgrids could stably support is finally obtained.

The paper is structured as follows: Section 2 analyzes control strategies for HESSs and CPLs and constructs an equivalent model of islanded DC microgrids. In Section 3, a nonlinear model is established based on the mixed potential function theory. Then, a large-signal stability criterion for islanded DC microgrids with $n+1$ parallel energy-storage converters is derived and optimized considering droop control. Sections 4 and 5 provide simulation and experimental results to verify the validity of the proposed large-signal stability criterion. Finally, Section 6 provides the conclusion.

2. Control Strategies and an Equivalent Model for Islanded DC Microgrids

Islanded DC microgrids consist of microsources, HESSs, and CPLs, as shown in Figure 1. The microsources mainly comprise renewable energy, such as wind and solar power. Wind generators and three-phase bridge rectifiers are cascaded to obtain DC power. A boost converter is used to increase the voltages of the PV units. The HESSs are composed of n batteries cascaded with bidirectional buck–boost converters and one SC which is also cascaded with buck–boost converters. In other words, there are $n+1$ parallel energy-storage converters in the HESS. Buck converters are adopted to support the DC loads. All closed-loop-controlled loads, such as converter loads and motor loads, are usually regarded as CPLs with negative impedance characteristics. When the DC bus voltage changes, the positive feedback introduced by the CPLs usually magnify these changes, resulting in instability.

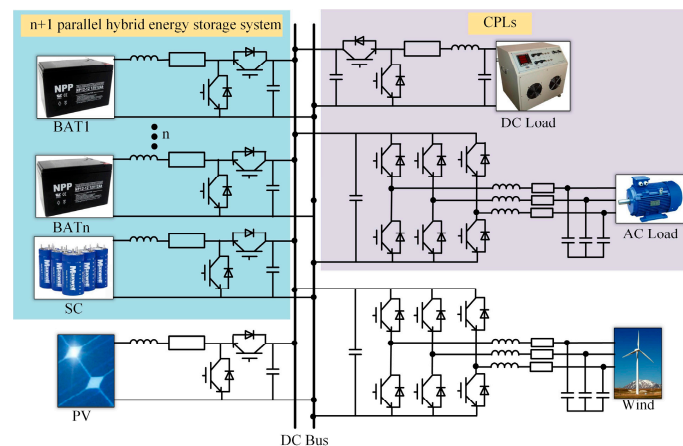


Figure 1. A simplified topology of a typical islanded DC microgrid.

2.1. Control Strategies for HESSs and CPLs

Firstly, the control strategies for a HESS are described. There are $n+1$ parallel energy storage converters in a HESS, but the control strategies for the n parallel battery converters are very different from the control strategy for the SC converter. Bidirectional buck–boost converters are mostly used in HESSs to achieve the simplest structure. A number of n batteries cascaded with bidirectional buck–boost converters in parallel connections are utilized to sustainably provide or absorb energy and eventually to keep the DC bus voltage constant. A SC cascaded with a bidirectional buck–boost converter is adopted to quickly output or input high-frequency power.

For the DC microgrid model, a droop control strategy based on the DC bus voltage is adopted which utilizes the coupling relationship between the output voltage and the output current to generate a V–I droop characteristic and form V–I droop control. The V–I droop control of a bidirectional DC–DC converter is such that the output voltage and current are controlled according to a specific correspondence, and the control equation is shown below.

The V–I droop control adopted by n parallel battery converters is shown as follows:

$$v_{refj} = v_{dc-ref} - k_j i_{batj} \quad (1)$$

In (1), v_{refj} is the reference DC bus voltage for the outer voltage loop of the j-th battery DC–DC converter. i_{batj} is the current of the j-th battery DC–DC converter, and k_j is the droop coefficient of the j-th battery DC–DC converter.

Generally, the droop coefficient k_j satisfies

$$\frac{\Delta v_{dcmin}}{i_{batmin}} \leq k_j \leq \frac{\Delta v_{dcmax}}{i_{batmax}} \tag{2}$$

In (2), Δv_{dcmax} and Δv_{dcmin} are the maximum voltage sag and minimum voltage sag, respectively. i_{batmax} and i_{batmin} are maximum current and minimum current of the battery DC–DC converter, respectively.

The droop coefficients are usually related to the currents of battery DC–DC converters, and are shown as

$$k_1 i_{bat1} = k_2 i_{bat2} = \dots = k_j i_{batj} = \dots = k_n i_{batn} \tag{3}$$

In (3), i_{batj} is the current of the j-th battery DC–DC converter, and k_j is the droop coefficient of the j-th battery DC–DC converter.

Based on (3), variable droop coefficients correspond to the variable currents of the battery DC–DC converters. Consequently, adjusting the droop coefficients allows one to obtain controllable currents for the battery DC–DC converters.

To eliminate the DC bus voltage sags introduced by the V–I droop control, voltage compensation Δv_{dc-ref} is added to the conventional droop control equation in (1) and is shown as

$$v_{refj} = v_{dc-ref} - k_j i_{batj} + \Delta v_{dc-ref} \tag{4}$$

According to (4), the reference DC bus voltage for the outer voltage loop of the j-th battery DC–DC converter is obtained. Similarly, the reference DC bus voltages of the n battery DC–DC converters are completely calculated. The n parallel battery converters are all controlled by inner current loops and outer voltage loops. The control strategies for n battery DC–DC converters are shown in Figure 2.

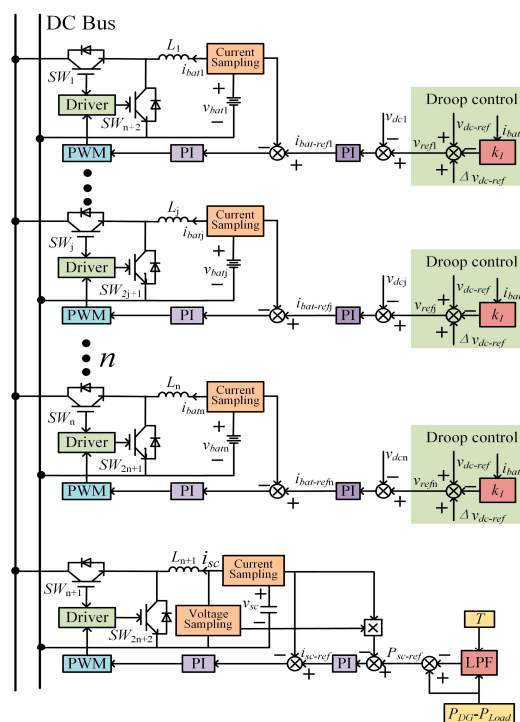


Figure 2. Control strategies for n+1 parallel converters in a HESS.

The V–I droop characteristic of a battery DC–DC converter is shown in Figure 3. According to the characteristic curve, the initial operation point is A; if the load power increases, the output current of the converter also increases, while the output voltage decreases, and finally, the operation point moves from A to B.

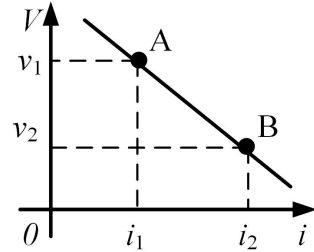


Figure 3. The characteristic curve of a V–I droop operation.

The objective of the n parallel battery converters is to keep the DC bus voltage constant, while the purpose of the SC converter is to absorb or supply high-frequency power.

Consequently, a low-pass filter (LPF) is utilized to obtain a high-frequency power difference between the microsources and CPLs, and the power is taken as the reference power P_{sc-ref} of the SC converter, as shown in Figure 4. The power of the microsources is P_{DG} , and the power of the CPLs is P_{load} . The filter time constant is T .

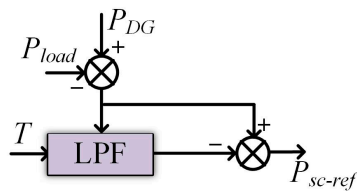


Figure 4. LPF control block diagram.

The transfer function of the LPF is:

$$H(s) = \frac{1}{T_S + 1} \tag{5}$$

In (5), T_S is the computational period, which is a fixed value during the filtering process.

According to Figure 4, the reference power of the SC converter is deduced, and is shown as

$$P_{sc-ref} = \frac{T_S}{T_S + 1} (P_{DG} - P_{load}) = \frac{T_S}{T_S + 1} P_{HESS} \tag{6}$$

After discretization, (6) is rewritten as follows:

$$P_{sc-ref}(k + 1) = \frac{T}{T + T_S} (P_{sc-ref}(k) + P_{HESS}(k + 1) - P_{HESS}(k)) \tag{7}$$

Let $P_{HESS}(k + 1) - P_{HESS}(k) = \Delta P_{HESS}$; thus, (7) is transferred into

$$P_{sc-ref}(k + 1) = \frac{T}{T + T_S} (P_{sc-ref}(k) + \Delta P_{HESS}) \tag{8}$$

Control strategies for the n battery buck–boost converters are shown in Figure 2. V–I droop control is utilized to achieve controllable battery currents without communications. Different droop coefficients introduce different battery currents. To eliminate DC bus voltage sags caused by V–I droop control, voltage compensation Δv_{dc-ref} is also added. Based on the current i_{batj} of the j-th battery buck–boost converter, the droop coefficient k_j of the j-th battery buck–boost converter, and the provided constant value v_{dc-ref} of the DC bus voltage, the reference DC bus voltage v_{refj} for the outer voltage loop of the j-th battery

buck–boost converter is obtained. Then, based on the outer voltage PI controllers and the inner current PI controllers, PWM signals are produced for n battery buck–boost converters.

The control strategy for the SC buck–boost converter is also shown in Figure 2. To absorb or supply high-frequency power, the LPF is utilized to obtain high-frequency power differences between the microsources and CPLs. The outer voltage PI controllers and inner current PI controllers are also utilized to generate PWM signals for the SC buck–boost converter.

The power characteristic of the CPLs is the most important parameter, and it can affect the stability of a DC microgrid. The buck converter and resistors controlled by the current control loop are used to represent typical CPLs. As the reference current varies, the power of the CPLs simultaneously changes. The CPL regulation feature is closely related to the proportional parameter of the current PI controller.

The control strategy for the CPLs is shown in Figure 5. v_{dc} is the DC bus voltage, and i_{ref} is the reference current of the CPLs. Based on the current PI controller, PWM signals are produced for the Buck converter.

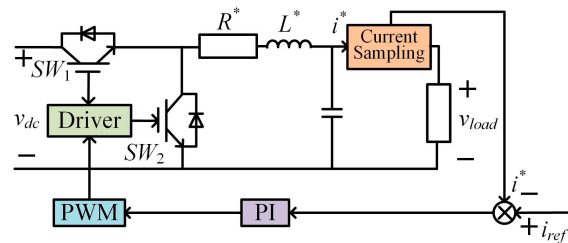


Figure 5. The control strategy for CPLs.

2.2. Equivalent Model of DC Microgrids

In islanded DC microgrids, microsources are modeled as power sources, and the power and current are P_{DG} and i_{DG} , respectively. The power and current of the CPLs are P_{load} and i_{dc} , respectively. Modeling a HESS is very complex, and models of n batteries with cascaded converters are different from the model of one SC with one cascaded converter.

As shown in Figure 6, when the battery is charging, the cascaded DC–DC converter operates in buck mode while Q_1 and D_2 are turned on, and the power flows from the DC bus to the battery. When the battery is discharging, the DC–DC converter operates in boost mode while Q_2 and D_1 are turned on, and the power flows from the battery to the DC bus.

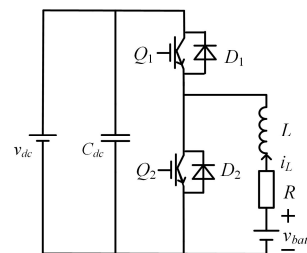


Figure 6. The topology of the bidirectional DC–DC converter circuit.

The differential equation of the battery DC–DC converter is

$$v_{dc} = \alpha v_{bat} - \alpha R i_L - \alpha L \frac{di_L}{dt} \tag{9}$$

In (9), v_{dc} is the DC bus voltage, v_{bat} is the battery voltage, i_L is the inductor current, R is the equivalent internal resistance of the battery, and α is the charging and discharging factor of the battery.

Consequently, based on (9), the battery and the cascaded DC–DC converter are equivalently modeled as a generalized battery, resistor, and inductor in series, as shown in Figure 7.

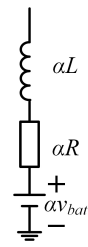


Figure 7. Equivalent model of one battery and one cascaded DC–DC converter.

When n batteries and cascaded DC–DC converters are connected in parallel, the differential equations are

$$\begin{cases} v_{dc1} = \alpha v_{bat1} - \alpha R i_{L1} - \alpha L \frac{di_{L1}}{dt} \\ \vdots \\ v_{dcj} = \alpha v_{batj} - \alpha R i_{Lj} - \alpha L \frac{di_{Lj}}{dt} \quad (j \in [1, n]) \\ \vdots \\ v_{dcn} = \alpha v_{batn} - \alpha R i_{Ln} - \alpha L \frac{di_{Ln}}{dt} \end{cases} \quad (10)$$

In (10), R_j is the equivalent internal resistance of the j -th battery.

Based on (10), the equivalent model of n batteries and cascaded DC–DC converters in parallel connections are derived and is shown in Figure 8.

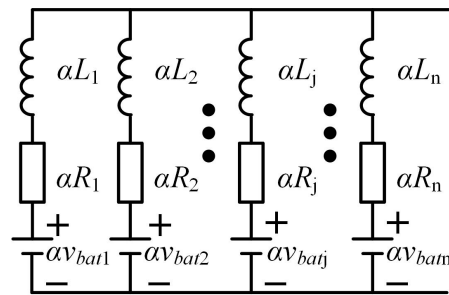


Figure 8. Equivalent model of n batteries and cascaded DC–DC converters in parallel connections.

The SC cascaded DC–DC converter is controlled by the outer power loop, and the power relationship of the SC and the cascaded DC–DC converter is as follows:

$$i_{sc} v_{dc} = i_{SC} v_{SC} = P_{sc} \quad (11)$$

In (11), i_{sc} is the output current of the SC’s DC–DC converter, v_{dc} is the DC bus voltage, v_{SC} and i_{SC} are the voltage and current of the SC, respectively, and P_{sc} is the power of the SC.

The equivalent model of the SC and the cascaded DC–DC converter is equivalent to a bidirectional power source and is shown in Figure 9.

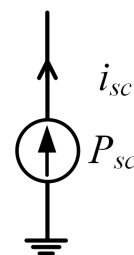


Figure 9. Equivalent model of the SC and the cascaded DC–DC converter.

Based on the equivalent models of the microsources, CPLs, and HESS, an equivalent model of the DC microgrids is established and is shown in Figure 10. R_j is the equivalent internal resistance of the j -th battery, α is the charging and discharging factor of the battery, L_j is the inductance of the j -th DC–DC converter, v_{batj} and i_{batj} are the voltage and current of the j -th battery, and P_{DG} , P_{sc} , and P_{load} are the power values of the microsources, the SC, and the CPLs, respectively. i_{DG} , i_{sc} , and i_{dc} are the currents of the microsources, the SC, and the CPLs, respectively. v_{dc} is the DC bus voltage, and C_{dc} is the filter capacitor.

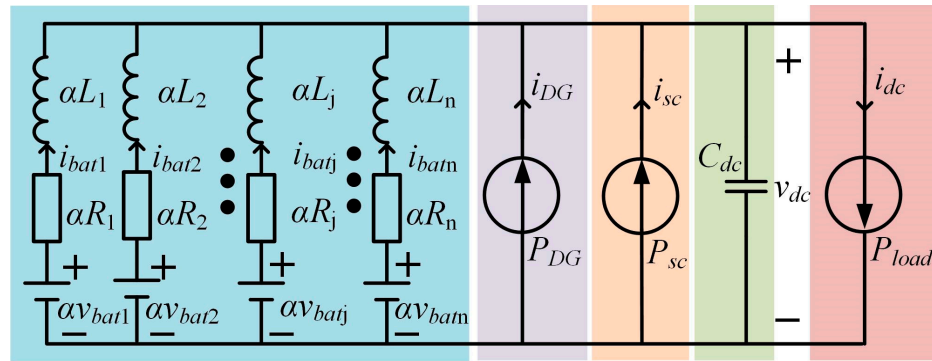


Figure 10. The equivalent model of the DC microgrids.

3. Nonlinear Model and Large-Signal Stability Criteria for Islanded DC Microgrids

The mixed potential function method is utilized to construct a nonlinear model and achieve a large-signal stability analysis of islanded DC microgrids.

Establishing a nonlinear model according to the mixed potential function is usually broken into three steps.

- (1) The voltage potential function or current potential function of the non-energy storage components is built.
- (2) The energy absorbed by the capacitor of the energy-storage element is obtained.
- (3) A formula is proposed based on the above process and converted into a standard form.

The mixed potential function $P(i, v)$ is related to the system structure, and its standard form is as follows:

$$P(i, v) = -A(i) + B(v) + (i, \gamma v - \alpha) \tag{12}$$

In (12), $A(i)$ is the current potential function, $B(v)$ is the voltage potential function, and $(i, \gamma v - \alpha)$ is determined by the system topology.

Formula (13) is used to verify the accuracy of (12).

$$\begin{cases} L \frac{di_\rho}{dt} = \frac{\partial P(i, v)}{\partial i_\rho} \\ C \frac{dv_\sigma}{dt} = -\frac{\partial P(i, v)}{\partial v_\sigma} \end{cases} \tag{13}$$

In (13), i_ρ and v_σ are the current variables and voltage variables of the inductors and capacitors.

The third stability theorem of the mixed potential function theory is often used to analyze large-signal stability. μ_1 is the minimum eigenvalue of $L^{-1/2} A_{ii}(i) L^{-1/2}$, μ_2 is the minimum eigenvalue of $C^{-1/2} B_{vv}(v) C^{-1/2}$, and $A_{ii}(i) = \partial^2 A(i) / \partial i^2$, $B_{vv}(v) = \partial^2 B(v) / \partial v^2$, $P_i = \partial P(i, v) / \partial i$, and $P_v = \partial P(i, v) / \partial v$.

If the systems satisfy Equation (14), there exists a convergence domain which causes the system trajectory to converge to the steady-state equilibrium operating point.

$$\mu_1 + \mu_2 \geq \delta, \delta > 0 \tag{14}$$

3.1. Conducting a Large-Signal Stability Analysis for Islanded DC Microgrids with n+1 Parallel Energy-Storage Converters

3.1.1. Large-Signal Model for Islanded DC Microgrids

According to the DC microgrid equivalent model in Figure 10, a large-signal model is established based on the mixed potential function theory.

The current potential function of the n batteries and cascaded DC–DC converters is obtained and shown as

$$P_i = \sum_{j=1}^n \alpha v_{batj} i_{batj} - \sum_{j=1}^n \frac{1}{2} \alpha i_{batj}^2 R_j \tag{15}$$

In (15), α is the charge and discharge factor of the batteries.

The voltage potential function of the microsources, the SC, and the cascaded DC–DC converter is

$$P_{v1} = P_{DG} - \int_0^{v_{dc}} \frac{P_{DG}}{v} dv + P_{sc} - \int_0^{v_{dc}} \frac{P_{sc}}{v} dv \tag{16}$$

The voltage potential function of the CPLs is

$$P_{v2} = -P_{load} + \int_0^{v_{dc}} \frac{P_{load}}{v} dv \tag{17}$$

The power potential function of the capacitor C_{dc} is

$$P_{v3} = v_{dc} \left(\frac{P_{load}}{v_{dc}} - \frac{P_{DG}}{v_{dc}} - \frac{P_{sc}}{v_{dc}} - \sum_{j=1}^n i_{batj} \right) \tag{18}$$

According to (16) to (18), the large-signal model of the DC microgrids with n+1 parallel energy-storage converters is

$$P(i, v) = \sum_{j=1}^n \alpha v_{batj} i_{batj} - \sum_{j=1}^n \frac{1}{2} \alpha i_{batj}^2 R_j - \int_0^{v_{dc}} \frac{P_{DG}}{v} dv - \int_0^{v_{dc}} \frac{P_{sc}}{v} dv + \int_0^{v_{dc}} \frac{P_{load}}{v} dv - v_{dc} \sum_{j=1}^n i_{batj} \tag{19}$$

In (19), v_{batj} and i_{batj} are the j-th battery’s voltage and current, R_j is the j-th battery’s equivalent internal resistance, P_{DG} is the microsource power, v_{dc} is the DC bus voltage, P_{sc} is the power of the SC, and P_{load} is the power of the CPLs.

Formula (12) is used to verify the mixed potential function derived for the DC microgrids in (19). It is proposed and shown as

$$\left\{ \begin{array}{l} \alpha L_1 \frac{di_{bat1}}{dt} = \alpha v_{bat1} - \alpha R_1 i_{bat1} - v_{dc} = \frac{\delta P(i,v)}{\delta i_{bat1}} \\ \vdots \\ \alpha L_j \frac{di_{batj}}{dt} = \alpha v_{batj} - \alpha R_j i_{batj} - v_{dc} = \frac{\delta P(i,v)}{\delta i_{batj}} \\ \vdots \\ \alpha L_n \frac{di_{batn}}{dt} = \alpha v_{batn} - \alpha R_n i_{batn} - v_{dc} = \frac{\delta P(i,v)}{\delta i_{batn}} \\ C_{dc} \frac{dv_{dc}}{dt} = -\frac{P_{DG}}{v_{dc}} - \frac{P_{sc}}{v_{dc}} + \frac{P_{load}}{v_{dc}} - \sum_{j=1}^n i_{batj} = -\frac{\delta P(i,v)}{\delta v_{dc}} \end{array} \right. \quad (j \in [1, n]) \tag{20}$$

Formula (20) meets the verification requirements of (13), verifying the validity of the large-signal model in (19).

Based on (19), the current potential function $A(i)$ is

$$A(i) = \begin{bmatrix} -\alpha v_{bat1} i_{bat1} + \frac{1}{2} \alpha i_{bat1}^2 R_1 & 0 & \cdots & 0 \\ 0 & \ddots & 0 & 0 \\ \vdots & 0 & \ddots & \vdots \\ 0 & 0 & \cdots & -\alpha v_{batn} i_{batn} + \frac{1}{2} \alpha i_{batn}^2 R_n \end{bmatrix} \tag{21}$$

Similarly, the voltage potential function $B(v)$ is

$$B(v) = \begin{bmatrix} -\int_0^{v_{dc}} \frac{P_{DG}}{v} dv - \int_0^{v_{dc}} \frac{P_{sc}}{v} dv + \int_0^{v_{dc}} \frac{P_{load}}{v} dv & 0 \\ 0 & 0 \end{bmatrix} \quad (22)$$

The quadratic partial derivatives of $A(i)$ and $B(v)$ are

$$A_{ii}(i) = \begin{bmatrix} -\frac{\partial \alpha v_{bat1}}{\partial i_{bat1}} + \alpha i_{bat1} & 0 & \cdots & 0 \\ 0 & \ddots & 0 & 0 \\ \vdots & 0 & \ddots & \vdots \\ 0 & 0 & \cdots & -\frac{\partial \alpha v_{batn}}{\partial i_{batn}} + \alpha i_{batn} \end{bmatrix} \quad (23)$$

$$B_{vv} = \begin{bmatrix} \frac{P_{DG}}{v_{dc}^2} + \frac{\partial i_{sc}}{\partial v_{dc}} + \frac{\partial i_{dc}}{\partial v_{dc}} & 0 \\ 0 & 0 \end{bmatrix} \quad (24)$$

3.1.2. Considering Control Parameters of Parallel Energy-Storage Converters and CPLs

According to the inner current control loop of the battery converters in Figure 2, it is derived and shown as

$$\begin{cases} \alpha v_{bat1} = v_{dc-ref} + k_{ip1} (i_{bat-ref1} - i_{bat1}) + k_{ii1} \int (i_{bat-ref1} - i_{bat1}) dt \\ \vdots \\ \alpha v_{batj} = v_{dc-ref} + k_{ipj} (i_{bat-refj} - i_{batj}) + k_{iij} \int (i_{bat-refj} - i_{batj}) dt \quad (j \in [1, n]) \\ \vdots \\ \alpha v_{batn} = v_{dc-ref} + k_{ipn} (i_{bat-refn} - i_{batn}) + k_{iin} \int (i_{bat-refn} - i_{batn}) dt \end{cases} \quad (25)$$

$$\begin{cases} \frac{\partial \alpha v_{bat1}}{\partial i_{bat1}} = -k_{ip1} \\ \vdots \\ \frac{\partial \alpha v_{batj}}{\partial i_{batj}} = -k_{ipj} \quad (j \in [1, n]) \\ \vdots \\ \frac{\partial \alpha v_{batn}}{\partial i_{batn}} = -k_{ipn} \end{cases} \quad (26)$$

In (25) and (26), k_{ipj} and k_{iij} are the proportional and integral parameters of the inner current loop of the j -th battery's DC-DC converter, v_{dc-ref} is the reference DC bus voltage, and $i_{bat-refj}$ is the reference current of the j -th battery DC-DC converter.

Based on the double control loops of the SC converter in Figure 2 and the power conservation principle, we obtain

$$i_{L2} = i_{SC} = k_{vp2} (P_{sc-ref} - i_{sc} v_{dc}) + k_{vi2} \int (P_{sc-ref} - i_{sc} v_{dc}) dt \quad (27)$$

$$i_{sc} v_{dc} = i_{SC} v_{SC} = P_{sc} \quad (28)$$

$$\frac{\partial i_{sc}}{\partial v_{dc}} = \frac{\partial \frac{i_{sc} v_{sc}}{v_{dc}}}{\partial v_{dc}} = \frac{-k_{vp2} i_{sc} v_{sc} v_{dc} - i_{SC} v_{SC}}{v_{dc}^2} = \frac{-(k_{vp2} v_{SC} + 1) P_{sc}}{v_{dc}^2} \quad (29)$$

In (27)–(29), k_{vp2} and k_{vi2} are the proportional and integral parameters of the outer power control loop of the SC DC-DC converter. v_{SC} and i_{SC} are voltage and current of the SC, and P_{sc-ref} and P_{sc} are the reference power and actual power of the SC converter, respectively.

According to the control model of CPLs, we obtain

$$d = k_{ip}^* (i_{ref}^* - i^*) + k_{ii}^* \int (i_{ref}^* - i^*) dt \tag{30}$$

$$P_{load} = i_{ref}^* v_{load} \tag{31}$$

$$i^* = \frac{dv_{dc} - v_{load}}{R^*} \tag{32}$$

In (30)–(32), k_{vp}^* and k_{vi}^* are the proportional and integral parameters of the outer voltage loop of the CPLs, and k_{pi}^* and k_{ii}^* are the proportional and integral parameters of the inner current loop of the CPLs. $v_{load-ref}$ is the reference voltage, and v_{load} is the actual voltage. i_{ref}^* is the reference current, and i^* is the actual current. R^* is the filter resistor.

Based on (30)–(32), we derive

$$i^* = \frac{k_{ip}^* i_{ref}^* v_{dc} - v_{load}}{R^* + k_{ip}^* v_{dc}} \tag{33}$$

$$i_{dc} = \frac{v_{load} i^*}{v_{dc}} = \frac{k_{ip}^* i_{ref}^* v_{dc} v_{load} - v_{load}^2}{R^* v_{dc} + k_{ip}^* v_{dc}^2} \tag{34}$$

Then, according to (34), (35) is proposed.

$$\frac{\partial i_{dc}}{\partial v_{dc}} = \frac{k_{ip}^* i_{ref}^* v_{load}}{R^* v_{dc} + k_{ip}^* v_{dc}^2} + \frac{(v_{load}^2 - k_{ip}^* i_{ref}^* v_{dc} v_{load})(R^* + 2k_{ip}^* v_{dc})}{(R^* v_{dc} + k_{ip}^* v_{dc}^2)^2} \tag{35}$$

3.1.3. Deriving the Large-Signal Stability Criterion of Islanded DC Microgrids

Based on the third stability theorem of the mixed potential theory in (14), the control characteristics of the battery DC–DC converter in (25), the control features of the SC converter in (27), and the control characteristics of the CPLs in (30), a large-signal stability criterion for islanded DC microgrids with n+1 parallel energy-storage converters is derived and shown as

$$\begin{cases} \mu_1 = \min \left(\frac{k_{ip1} + \alpha R_1}{\alpha L_1}, \frac{k_{ip2} + \alpha R_2}{\alpha L_2}, \dots, \frac{k_{ipj} + \alpha R_j}{\alpha L_j}, \dots, \frac{k_{ipn} + \alpha R_n}{\alpha L_n} \right) \\ \mu_2 = \frac{P_{DG} - \frac{T}{T+T_S} (P_{sc-ref}(k) + \Delta P_{HESS}) (k_{vp2} v_{SC} + 1)}{C_{dc} v_{dc}^2} + \frac{k_{ip}^* P_{load}}{C_{dc} (R^* v_{dc} + k_{ip}^* v_{dc}^2)} + \frac{(v_{load}^2 - k_{ip}^* v_{dc} P_{load})(R^* + 2k_{ip}^* v_{dc})}{C_{dc} (R^* v_{dc} + k_{ip}^* v_{dc}^2)^2} \quad (j \in [1, n]) \\ \mu_1 + \mu_2 > 0 \end{cases} \tag{36}$$

As shown in (36), this manuscript considers the microsource power P_{DG} , the CPLs power P_{load} , the computational period T_s of the low-pass filter, the inductors L_j , the capacitors C_{dc} , the DC bus voltage v_{dc} , the battery charging and discharging factor α , the equivalent internal resistances R_j of the batteries, the proportional parameters k_{ipj} of the inner current loop of the n battery DC–DC converters, the proportional parameter k_{vp2} of the outer power control loop of the SC DC–DC converter, and the proportional parameter k_{ip}^* of the CPLs' inner current loop, and provides quantitative constraints to guarantee the large-signal stability of islanded DC microgrids.

Unfortunately, μ_1 and μ_2 are the second partial derivatives of $A(i)$ and $B(v)$, and this calculation procedure neglects the power differences introduced via the use of droop control for the n battery converters. The proposed criterion in (36) is conservative.

3.2. Optimizing the Large-Signal Stability Criteria of Islanded DC Microgrids Based on Droop Control

Thevenin’s theorem is adopted to obtain the equivalent model of n parallel batteries and cascaded converters in [37].

It is assumed that the batteries are all ideal, and the voltage satisfies $v_1 = v_2 = \dots = v_j = \dots = v_n$. The traditional equivalent model of n parallel batteries and cascaded converters is shown in Figure 11. Based on Thevenin’s theorem, the elements in the blue parts of Figure 11 are modeled as a general battery v_1 with an equivalent resistor R_{eq} and an inductor L_{eq} , and they satisfy

$$R_{eq} = \frac{(R_1 + R_2 + \dots + R_j + \dots + R_n)}{R_1 R_2 \dots R_j \dots R_n} \tag{37}$$

$$L_{eq} = \frac{(L_1 + L_2 + \dots + L_j + \dots + L_n)}{L_1 L_2 \dots L_j \dots L_n} \tag{38}$$

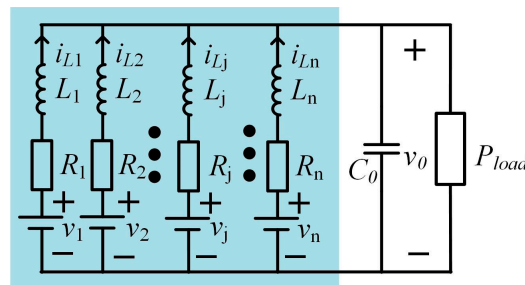


Figure 11. The traditional equivalent model of n parallel batteries and cascaded converters.

Based on (37) and (38), an optimized equivalent model of n parallel batteries and cascaded converters based on Thevenin’s theorem is shown in Figure 12.

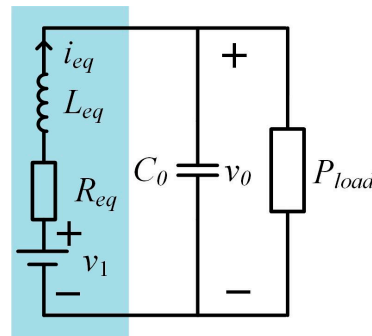


Figure 12. An optimized equivalent model of n parallel batteries and cascaded converters based on Thevenin’s theorem.

For the traditional model in Figure 11, the third stability theorem of mixed potential theory is applied to obtain the minimum eigenvalue μ'_1 , which is shown as

$$\mu'_1 = \min \left(\frac{R_1}{L_1}, \frac{R_2}{L_2}, \dots, \frac{R_j}{L_j}, \dots, \frac{R_n}{L_n} \right) \tag{39}$$

For the optimized model in Figure 12, the minimum eigenvalue μ''_1 is also deduced and shown as

$$\mu''_1 = \min \left(\frac{R_{eq}}{L_{eq}} \right) = \frac{R_{eq}}{L_{eq}} \tag{40}$$

According to (37) and (38), (40) is transferred into

$$\begin{aligned} \mu_1'' &= \min\left(\frac{R_{eq}}{L_{eq}}\right) = \frac{R_{eq}}{L_{eq}} = \frac{1/(1/R_1+1/R_2+\dots+1/R_j+\dots+1/R_n)}{1/(1/L_1+1/L_2+\dots+1/L_j+\dots+1/L_n)} \\ &= \frac{1/R_1}{1/R_1+1/R_2+\dots+1/R_j+\dots+1/R_n} \cdot \frac{R_1}{L_1} + \dots + \\ &\quad \frac{1/R_j}{1/R_1+1/R_2+\dots+1/R_j+\dots+1/R_n} \cdot \frac{R_j}{L_j} + \dots + \\ &\quad \frac{1/R_n}{1/R_1+1/R_2+\dots+1/R_j+\dots+1/R_n} \cdot \frac{R_n}{L_n} \\ &= m_1 \cdot \frac{R_1}{L_1} + \dots + m_j \cdot \frac{R_j}{L_j} + \dots + m_n \cdot \frac{R_n}{L_n} \quad (j \in [1, n]) \end{aligned} \tag{41}$$

$$m_j = \frac{1/k_j}{1/k_1 + \dots + 1/k_j + \dots + 1/k_n} \quad (j \in [1, n]) \tag{42}$$

The weight coefficient m_j of the j -th battery's DC-DC converter is introduced to simplify (41) and is shown as

$$\mu_1'' = \sum_{j=1}^n m_j \cdot \frac{R_j}{L_j} \tag{43}$$

Equation (43) indicates that the droop coefficients related to m_j are also considered, making the optimized equivalent model and the large-signal stability analysis more consistent with actual DC microgrids.

Similarly, an optimized equivalent model of islanded DC microgrids with $n+1$ parallel batteries and cascaded converters is established, and based on Thevenin's theorem, an optimized large-signal stability criterion is proposed and shown as

$$\left\{ \begin{aligned} \mu_1 &= \sum_{j=1}^n m_j \left(\frac{k_{ipj} + \alpha R_j}{\alpha L_j} \right) \\ \mu_2 &= \frac{P_{DG} - \frac{T}{T+T_S} (P_{sc-ref}(k) + \Delta P_{HESS}) (k_{vp2} v_{sc} + 1)}{C_{dc} v_{dc}^2} + \frac{k_{ip}^* P_{load}}{C_{dc} (R^* v_{dc} + k_{ip}^* v_{dc}^2)} + \frac{(v_{out}^2 - k_{ip}^* v_{dc} P_{load}) (R^* + 2k_{ip}^* v_{dc})}{C_{dc} (R^* v_{dc} + k_{ip}^* v_{dc}^2)^2} \\ \mu_1 + \mu_2 &> 0 \end{aligned} \right. \tag{44}$$

Based on the droop control of n battery DC-DC converters, Thevenin's theorem is utilized to optimize the derived large-signal stability criteria of the islanded DC microgrids in (36), and the optimized large-signal stability criterion is shown as in (44). It is obvious that microsource power P_{DG} , the CPL power P_{load} , the computational period of the LPF T_s , the inductors L_j , the capacitors C_{dc} , the DC bus voltage v_{dc} , the battery charging and discharging factor α , the equivalent internal resistances R_j of the batteries, the proportional parameters k_{ipj} of the inner current loop of the n battery DC-DC converters, the proportional parameter k_{vp2} of the outer power control loop of the SC DC-DC converter, the proportional parameter k_{ip}^* of the CPLs' inner current loop, and the weight coefficient m_j related to the droop coefficients, all affect the large-signal stability of islanded DC microgrids with $n+1$ parallel energy-storage converters.

In (44), the control parameter k_{ip}^* of the CPLs is introduced, significantly improving the conservatism of the derived stability criterion. Furthermore, droop coefficients are always considered during modeling and derivation. Consequently, compared with (36), the optimized large-signal stability criterion in (44) is more applicable to analysis of the large-signal stability of actual DC microgrids.

3.3. Comparisons

Based on (36), the maximum CPL power that the islanded DC microgrids can stably support is derived and shown in (45). According to (45), if variable CPL power values are always lower than the maximum value, the islanded DC microgrids will operate stably. In addition, as the microsource power P_{DG} , the proportional parameters k_{ipj} of the inner current loop of the n battery DC-DC converters, and the proportional parameter k_{vp2} of the outer power control loop of the SC DC-DC converter become bigger, the allowable

maximum CPL power values that the islanded DC microgrids can stably support increase. On the contrary, when the proportional parameter k_{ip}^* of the CPLs' inner current loop increases, the allowable maximum CPL power values that the islanded DC microgrids can stably support decrease. If the CPLs are modeled ideally as before, which means that the proportional parameter k_{ip}^* of the CPLs' inner current loop is infinitely large, the obtained maximum CPL power that the islanded DC microgrids can stably support is absolutely reduced. Consequently, considering the regulation of CPLs instead of ideal modeling could significantly improve the conservatism of the proposed criteria.

$$P_{load} < \left[P_{DG} - \frac{T}{T+T_S} \left(P_{sc-ref}(k) + \Delta P_{HESS} \right) (k_{vp2} v_{SC} + 1) \right] \cdot \left(\frac{R^*}{k_{ip}^* v_{dc}} + 2R^* + k_{ip}^* v_{dc} \right) + \min \left(\frac{k_{ip1} + \alpha R_1}{\alpha L_1}, \frac{k_{ip2} + \alpha R_2}{\alpha L_2}, \dots, \frac{k_{ipj} + \alpha R_j}{\alpha L_j}, \dots, \frac{k_{ipn} + \alpha R_n}{\alpha L_n} \right) \cdot C_{dc} \left(\frac{R^*}{k_{ip}^*} + 2R^* v_{dc} + k_{ip}^* v_{dc}^2 \right) + \frac{R^* v_{load}^2}{k_{ip}^* v_{dc}^2} + \frac{2v_{load}^2}{v_{dc}} \quad (45)$$

When comparing (36) and (44), the largest difference is found in μ_1 . In (36), only the minimum equivalent internal resistances of the batteries and the minimum proportional parameters of the inner current loop of the n battery DC–DC converters are taken into account, and the equivalent internal resistances of other batteries and control parameters are all neglected. This really introduces the conservatism of the proposed large-signal stability criteria in (36). However, in (44), weight coefficients related to the droop control coefficients are presented, and n equivalent internal resistances of the batteries and n proportional parameters of the inner current loop of the n battery DC–DC converters are all considered, definitely decreasing the conservatism. Consequently, the optimized large-signal stability criteria of islanded DC microgrids in (44) are more consistent with practical DC microgrids.

Similarly, the maximum CPL power values are also derived based on (44) and shown in (46). Comparing (45) and (46), there are many common parameters. When the microsource power P_{DG} , the proportional parameters k_{ipj} of the inner current loop of the n battery DC–DC converters, and the proportional parameter k_{vp2} of the outer power control loop of the SC DC–DC converter become larger, the allowable maximum CPL power that the islanded DC microgrids can stably support increases. When the proportional parameter k_{ip}^* of the CPLs' inner current loop decreases, the allowable maximum CPL power that islanded DC microgrids can stably support also increases.

$$P_{load} < \left[P_{DG} - \frac{T}{T+T_S} \left(P_{sc-ref}(k) + \Delta P_{HESS} \right) (k_{vp2} v_{SC} + 1) \right] \cdot \left(\frac{R^*}{k_{ip}^* v_{dc}} + 2R^* + k_{ip}^* v_{dc} \right) + \sum_{j=1}^n m_j \left(\frac{k_{ipj} + \alpha R_j}{\alpha L_j} \right) \cdot C_{dc} \left(\frac{R^*}{k_{ip}^*} + 2R^* v_{dc} + k_{ip}^* v_{dc}^2 \right) + \frac{R^* v_{load}^2}{k_{ip}^* v_{dc}^2} + \frac{2v_{load}^2}{v_{dc}} \quad (46)$$

4. Simulation Verification

To verify the correctness of the proposed large-signal stability criterion for islanded DC microgrids with n+1 parallel energy-storage converters in (44), two battery converters connected in parallel with one SC converter are taken as a typical example.

Based on Figures 2 and 5, Matlab R2020a/Simulink software is adopted to construct a simulation model of islanded DC microgrids with three parallel energy-storage converters, and the simulation parameters are shown in Table 1. The batteries are connected to the DC bus through two bidirectional DC–DC converters. The outer voltage control loop and the inner current control loop are utilized in these converters. Droop control is adopted to distribute power between the two batteries' cascaded converters. The outer power control loop and the inner current control loop are employed in the SC cascaded converter to absorb or release high-frequency power based on the LPF. The microsourses are represented by a power source. The CPLs are modeled as a closed-loop-controlled converter and a resistor.

Table 1. Simulation parameters of islanded DC microgrids with three parallel energy-storage converters.

Parameters	Value
DC bus voltage (v_{dc})	400 V
Battery voltage (v_{bat})	150 V
SC voltage (v_{sc})	160 V
CPL voltage (v_{load})	200 V
Droop coefficient of battery 1's DC–DC converter (k_1)	0.5
Droop coefficient of battery 2's DC–DC converter (k_2)	0.25
Filter capacitor (C_{dc})	3 mF
Inductor (L_1)	5 mH
Inductor (L_2)	5 mH
Inductor (L_3)	5 mH
Microsource power (P_{DG})	4 kW
Initial power of CPLs (P_{load})	20 kW

According to (44), the stability influences of the different CPL power values and the different control parameters of two parallel battery converters are analyzed separately.

4.1. Large-Signal Stability Analysis of Islanded DC Microgrids under Different CPL Power Variations

To verify the stability of the islanded DC microgrids with three parallel energy-storage converters, two groups with different CPLs are introduced based on (44), and shown in Table 2. The control parameters of the two groups are the same. However, the variations in the power of the CPLs in Group A satisfy (44), while the variations in the power of the CPLs in Group B do not satisfy it. At 1.5 s, CPL power variations occur in both situations.

Table 2. Simulation parameters of Groups A and B.

Parameters	A	B
Proportional parameter of the inner current loop belonging to the first battery's DC–DC converters, k_{ip1}	4	4
Proportional parameter of the inner current loop belonging to the second battery's DC–DC converters, k_{ip2}	4	4
Proportional parameter of the outer power loop of the SC's DC–DC converter, k_{vp2}	15	15
The power variations of CPLs, P_{load}	20 kW → 40 kW	20 kW → 60 kW
Meeting large-signal stable criterion in (44)	Yes	No

Waveforms of the CPLs' power, the DC bus voltage, and the power values of battery 1, battery 2, and the SC when the parameters in Group A are applied are all shown in Figure 13. At 1.5 s, the power of the CPLs changes from 20 kW to 40 kW, and the SC immediately responds by releasing peak power. During this period, the power values of batteries 1 and 2 both increase slowly, and the DC bus voltage returns to 400 V after a brief fluctuation. The simulation results in Figure 13 indicate that the parameters in Group A could guarantee that islanded DC microgrids with three parallel energy-storage converters would be stable during large disturbances.

Then, the waveforms of power of the CPLs, the DC bus voltage, and the power values of battery 1, battery 2, and the SC when the parameters in Group B are adopted are all shown in Figure 14. At 1.5 s, the power of the CPLs changes from 20 kW to 60 kW; unfortunately, violent power oscillations appear. Furthermore, large oscillations also occur in the DC bus voltage and the power values of the batteries and the SC. Figure 14 demonstrates that the parameters in Group B could not guarantee that the islanded DC microgrids with three parallel energy-storage converters would be stable during large disturbances.

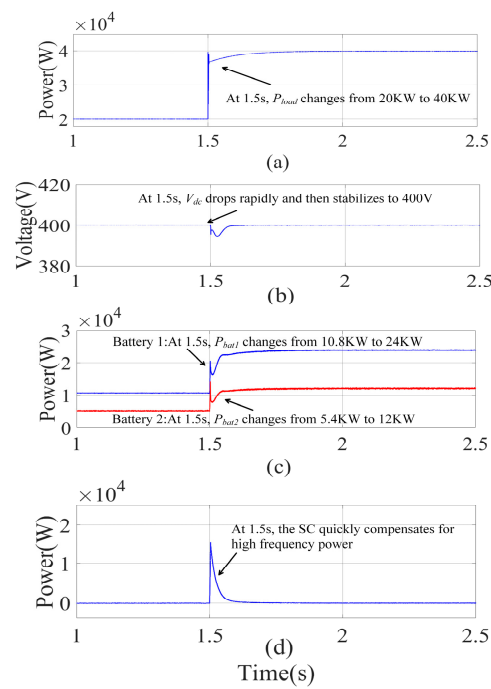


Figure 13. Simulation results when Group A is used. (a) The CPLs' power, (b) DC bus voltage, (c) the power of battery 1 and battery 2, and (d) the SC's power.

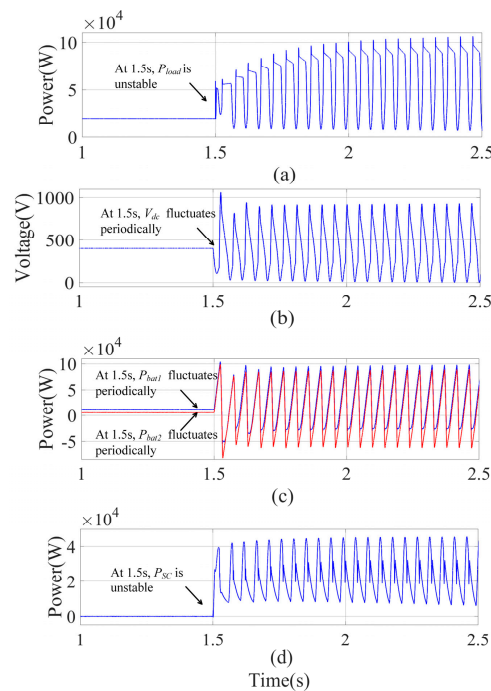


Figure 14. Simulation results when Group B is utilized. (a) The CPLs' power, (b) DC bus voltage, (c) the power of battery 1 and battery 2, and (d) the SC's power.

Based on the simulation results in Figures 13 and 14, if the parameters of islanded DC microgrids with three parallel energy-storage converters satisfy (44), the system would return to a stable condition after large disturbances. On the contrary, when the parameters of islanded DC microgrids with three parallel energy-storage converters do not satisfy (44), the system is unstable when large disturbances occur. Consequently, the validity of (44) is verified.

4.2. Large-Signal Stability Analysis of Islanded DC Microgrids under Different Control Parameters of Battery Converters

Based on (44), Groups C and D, with different proportional parameters of the inner current loop belonging to the battery DC–DC converters, are designed to analyze the stability of islanded DC microgrids with three parallel energy-storage converters. The parameters of Group C and D are shown in Table 3. The control parameters in Group C satisfy (44), while the control parameters in Group D do not satisfy it. At 1.5 s, control parameter changes occur in both situations.

Table 3. Simulation parameters of Groups C and D.

Parameters	C	D
Proportional parameter of the inner current loop belonging to the first battery DC–DC converters, k_{ip1}	4	0.2
Proportional parameter of the inner current loop belonging to the second battery DC–DC converters, k_{ip2}	4	0.2
Proportional parameter of the outer power loop of the SC DC–DC converter, k_{vp2}	15	15
The power variations of CPLs, P_{load}	20 kW → 40 kW	20 kW → 40 kW
Meeting large-signal stable criterion in (44)	Yes	No

Waveforms of the CPLs’ power step, DC bus voltage, battery 1 power, battery 2 power, and SC power when the Group C parameters are utilized are shown in Figure 15. At 1.5 s, the power of the CPLs changes from 20 kW to 40 kW, and the SC immediately responds by releasing peak power. During the period, the power values of batteries 1 and 2 both increase slowly, and after a brief fluctuation, the DC bus voltage returns to 400 V. the simulation results in Figure 15 indicate that the parameters in Group C could guarantee that islanded DC microgrids with three parallel energy-storage converters remain stable during large disturbances.

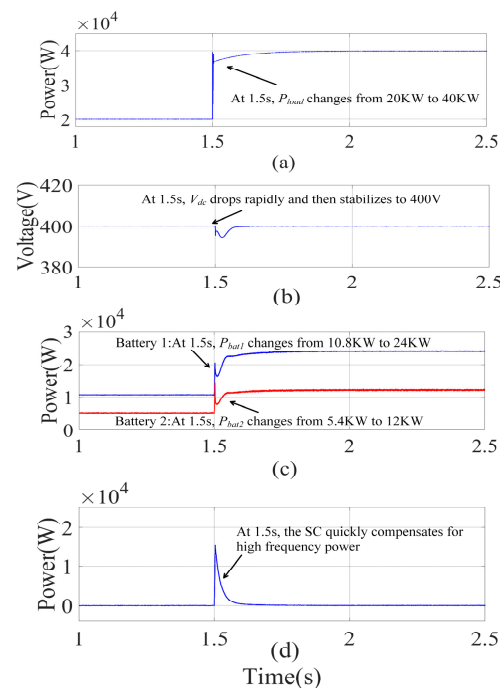


Figure 15. Simulation results when Group C is adopted. (a) The CPLs’ power, (b) DC bus voltage, (c) the power of battery 1 and battery 2, and (d) the SC’s power.

Waveforms of the CPLs' power step, the DC bus voltage, battery 1 power, battery 2 power, and SC power when the Group D parameters are utilized are shown in Figure 16. At 1.5 s, the power of the CPLs changes from 20 kW to 40 kW; unfortunately, violent power oscillations appear. Additionally, the DC bus voltage and the power values of the batteries and the SC all suffer from large oscillations. The simulation results shown in Figure 16 show that the Group D parameters could not guarantee that islanded DC microgrids with three parallel energy-storage converters remain stable during large disturbances.

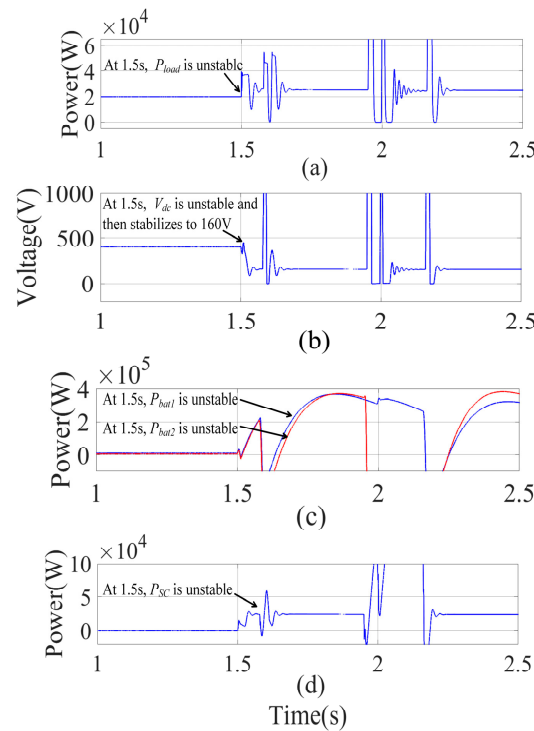


Figure 16. Simulation results when Group D is employed. (a) CPLs' power, (b) DC bus voltage, (c) the power of battery 1 and battery 2, and (d) the SC's power.

Comparing the simulation results in Figures 15 and 16, it can be seen that when the control parameters meet the proposed stability criterion in (44), the stability of islanded DC microgrids with three parallel energy-storage converters would be ensured during large disturbances. Otherwise, if the parameters do not satisfy (44), islanded DC microgrids could not maintain a stable state. Consequently, the derived stability criterion in (44) is correct.

The simulation results in Figures 13–16 verify the validity of the proposed large-signal stability criterion for islanded DC microgrids with $n+1$ parallel energy-storage converters in (44).

5. Experimental Results

Based on Figures 2 and 5, an experimental platform of islanded DC microgrids with three parallel energy-storage converters was constructed and is shown in Figure 17 in order to verify the feasibility of the derived large-signal stability criterion in (44).

The constructed islanded DC microgrids consist of microsources, HESSs, and CPLs, and the parameters are shown in Table 4. The microsources are represented by a DC power supply to output constant power. The desired power values of the CPLs are achieved by regulating the reference values of the load converter. V–I droop control is adopted to produce reference voltages for the outer voltage control loop of two energy-storage converters and to keep the DC bus voltage constant. A LPF is utilized to obtain a high-frequency power difference between the microsources and CPLs, and the power is taken as

the reference power of the SC converter’s outer power loop. A DSP-TMS320F28335 is used as the controller for the parallel energy-storage converters.

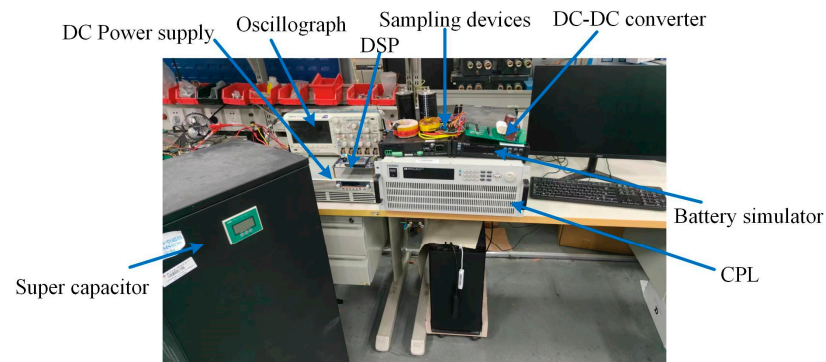


Figure 17. Experimental platform of islanded DC microgrids.

Table 4. Experimental parameters of islanded DC microgrids with three parallel energy-storage converters.

Parameters	Value
DC bus voltage (v_{dc})	60 V
Battery voltage (v_{bat})	36 V
SC voltage (v_{sc})	24 V
CPLs’ voltage (v_{load})	48 V
Droop coefficient of battery 1 DC–DC converter (k_1)	0.5
Droop coefficient of battery 2 DC–DC converter (k_2)	0.25
Filter capacitor (C_{dc})	2.2 mF
Inductor (L_1)	4.44 mH
Inductor (L_2)	4.44 mH
Inductor (L_3)	2.95 mH

Similarly, according to (44), the stability influences of different CPL power values and different control parameters for the two parallel battery converters are analyzed respectively.

5.1. Large-Signal Stability Analysis of Islanded DC Microgrids with Different CPL Values

To verify the stability of islanded DC microgrids with three parallel energy-storage converters, two groups with different CPL powers are introduced based on (44) and shown in Table 5. The control parameters of the two groups are the same. Unfortunately, the power variations of the CPLs in Group E satisfy (44), while the power variations of the CPLs in Group F do not satisfy it. At 1.5 s, variations in the power of the CPLs appear in both situations.

Table 5. Experimental parameters of Groups E and F.

Parameters	E	F
Proportional parameter of the inner current loop belongs to the first battery’s DC–DC converters, k_{ip1}	0.4	0.4
Proportional parameter of the inner current loop belongs to the second battery’s DC–DC converters, k_{ip2}	0.4	0.4
Proportional parameter of the outer power loop of the SC DC–DC converter, k_{vp2}	1.2	1.2
The power of the CPLs, P_{load}	50 kW → 150 W	50 kW → 210 W
Satisfying large-signal stability criterion in (44)	Yes	No

Curves of the CPL current, the DC bus voltage, and the currents of battery 1, battery 2, and the SC when the parameters in Group E are utilized are all shown in Figure 18. At 1.5 s,

the power of the CPLs changes from 50 W to 150 W, and the SC immediately releases a current. During this period, the currents of batteries 1 and 2 both increase slowly and then remain constant. The DC bus voltage remains stable after a small fluctuation. Figure 18 illustrates that the parameters in Group E could guarantee that islanded DC microgrids with three parallel energy-storage converters remain stable during large disturbances.

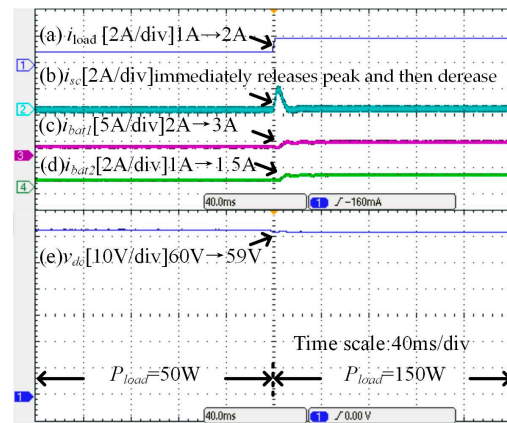


Figure 18. Experimental results when Group E is employed. (a) The CPL current, (b) the SC’s current, (c) the current of battery 1, (d) the current of battery 1, and (e) the DC bus voltage.

Then, the waveforms of the CPL current, DC bus voltage, and the currents of battery 1, battery 2, and the SC when the parameters in Group E are adopted are all shown in Figure 19. At 1.5 s, the power of the CPLs changes from 50 W to 210 W, the SC immediately releases a peak current, and the batteries’ currents increase gradually. However, the DC bus voltage continuously drops and is not able to return to the rated value. The voltage error between the rated value and the final value is more than 5%. Figure 14 demonstrates that the parameters in Group F could not guarantee that islanded DC microgrids with three parallel energy-storage converters remain stable during large disturbances.

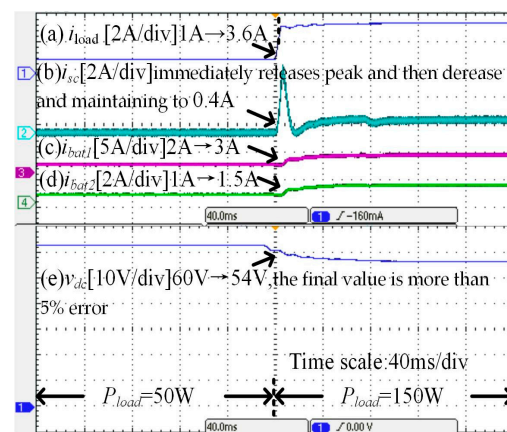


Figure 19. Experimental results when Group F is used. (a) The CPL current, (b) the SC’s current, (c) the current of battery 1, (d) the current of battery 1, and (e) the DC bus voltage.

Based on the comparison of Figures 18 and 19, if the parameters of islanded DC microgrids with three parallel energy-storage converters satisfy (44), the system would return to a stable condition after large disturbances. On the contrary, when the parameters of islanded DC microgrids with three parallel energy-storage converters do not satisfy (44), the system is unstable when large disturbances occur. The experimental results in Figures 18 and 19 coincide with the simulation results in Figures 13 and 14. Consequently, the validity of (44) is verified.

5.2. Large-Signal Stability Analysis of Islanded DC Microgrids When Different Control Parameters for Battery Converters Are Utilized

To verify the stability of islanded DC microgrids with three parallel energy-storage converters, two groups with different control parameters for energy-storage converters are introduced based on (44) and shown in Table 6. The control parameters in Group G satisfy (44), while the power variations of the CPLs in Group H do not satisfy it. At 1.5 s, the variations in the power of the CPLs from 50 W to 150 W occur in both situations.

Table 6. Experimental parameters of Groups G and H.

Parameters	G	H
Proportional parameter of the inner current loop belonging to the first battery’s DC–DC converters, k_{ip1}	2.2	0.1
Proportional parameter of the inner current loop belonging to the second battery’s DC–DC converters, k_{ip2}	2.2	0.1
Proportional parameter of the outer power loop of the SC DC–DC converter, k_{vp2}	4.5	4.5
The power of CPLs, P_{load}	50 kW → 150 W	50 kW → 150 W
Satisfying large-signal stability criterion in (44)	Yes	No

Waveforms of the CPLs’ current, the DC bus voltage, and the currents of battery 1, battery 2, and the SC when the parameters in Group G are applied are shown in Figure 20. At 1.5 s, the power of the CPLs changes from 50 W to 150 W, and the SC immediately releases power. The currents of batteries 1 and 2 both increase slowly, and the DC bus voltage returns to 60 V after a fluctuation. The experimental results in Figure 20 indicate that the parameters in Group G could ensure that islanded DC microgrids with three parallel energy-storage converters remain stable during large disturbances.

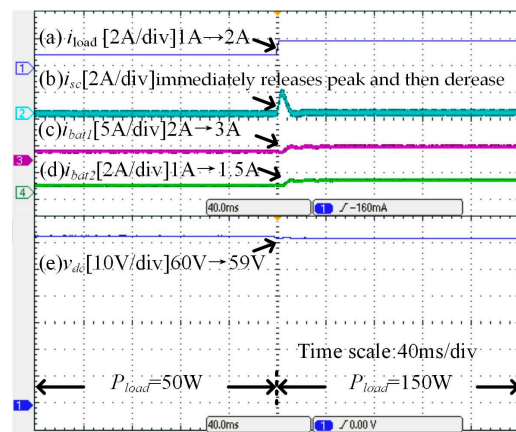


Figure 20. Experimental results when Group G is utilized. (a) The CPLs’ current, (b) the SC’s current, (c) the current of battery 1, (d) the current of battery 2, and the (e) DC bus voltage.

Then, curves of the CPLs’ current, the DC bus voltage, and the currents of battery 1, battery 2, and the SC are all shown in Figure 21. At 1.5 s, the CPLs’ power increases from 50 W to 150 W; unfortunately, violent current oscillations of the batteries appear. The battery currents cannot return to a stable state. Figure 21 shows that the parameters in Group H could not guarantee that islanded DC microgrids with three parallel energy-storage converters remain stable during large disturbances.

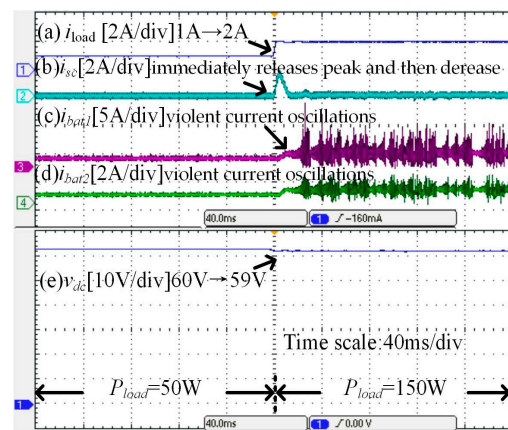


Figure 21. Experimental results when Group H is employed. (a) The CPLs' current, (b) the SC's current, (c) the current of battery 1, (d) the current of battery 1, and (e) the DC bus voltage.

Comparing of Figures 20 and 21, if parameters of islanded DC microgrids with three parallel energy-storage converters satisfy (44), the system would return stable after large disturbances. On the contrary, when parameters of islanded DC microgrids with three parallel energy-storage converters do not satisfy (44), the system is unstable when large disturbances occur. The experimental results in Figures 20 and 21 coincide with simulation results in Figures 13 and 15. Consequently, the correctness of (44) is identified.

The experimental results in Figures 18–21 validate the validity of the derived large-signal stability criterion for islanded DC microgrids with $n+1$ parallel energy-storage converters in (44).

6. Conclusions

Firstly, an equivalent model of islanded DC microgrids with $n+1$ parallel energy-storage converters is constructed based on control strategies for converters. Then, the mixed potential function theory is utilized to derive large-signal stability criterion. Droop control for n battery converters is adopted to optimize the stability criterion. The optimized stability criteria indicate that the microsource power P_{DG} , the CPLs' power P_{load} , the filter time constant T , the computational period T_s , the inductors L_j , the capacitors C_{dc} , the DC bus voltage v_{dc} , the battery charging and discharging factor α , the equivalent internal resistances R_j of the batteries, the proportional parameters k_{ipj} of the inner current loop of the n battery DC–DC converters, the proportional parameter k_{vp2} of the outer power control loop of the SC DC–DC converter, the proportional parameter k_{ip}^* of the CPLs' inner current loop, and the weight coefficient m_j related to the droop coefficients all affect the large-signal stability of islanded DC microgrids with $n+1$ parallel energy-storage converters. Furthermore, on the basis of the presented large-signal stability criteria, the maximum CPL power that islanded DC microgrids can stably support is obtained. Finally, simulation and experimental results verify the correctness of the provided large-signal stability criterion for islanded DC microgrids with $n+1$ parallel energy-storage converters.

The proposed large-signal stability criteria and obtained maximum CPL powers are extremely useful in many applications. When planning an islanded DC microgrid, to obtain a large maximum CPL power that the system can support, small inductors, a large DC bus capacitor, and proportional parameters are utilized, which could absolutely ensure the large-signal stability of the system in advance. On the other hand, when more sources and loads are connected to the existing islanded microgrids, new allowable maximum CPL power values are derived considering primary sources, new sources, and other system parameters. If the new allowable maximum CPL power is not large enough, by regulating battery converter parameters, new islanded microgrids with increased capacity can also guarantee large-signal stability, and furthermore, enough stability margins can also be obtained.

Author Contributions: Study design, literature search, and writing the manuscript, X.L.; graph production, data analysis, and data processing, Y.Z.; supervision and data collection, Y.S.; resources and writing—review and editing, X.S.; translation and literature search, J.Z. All authors have read and agreed to the published version of the manuscript.

Funding: This project received support from the National Key R&D Program of China, Grant/Award Number 2021YFE0103800, and the Organized Scientific Research Project of North China University of Technology, Grant/Award Number 2023YZZKY05.

Data Availability Statement: Data are available from the authors.

Conflicts of Interest: The authors declare no conflict of interest.

References

1. Dragičević, T.; Lu, X.; Vasquez, J.C.; Guerrero, J.M. DC Microgrids—Part I: A Review of Control Strategies and Stabilization Techniques. *IEEE Trans. Power Electron.* **2016**, *31*, 4876–4891.
2. Lin, P.; Jiang, W.; Tu, P.; Jin, C.; Zhang, C.; Wang, P. Self-Disciplined Large Signal Stabilizer Design for Hybrid Energy Storage System in Renewable DC Power Systems. *IEEE Trans. Sustain. Energy* **2020**, *11*, 2345–2355. [[CrossRef](#)]
3. Mutarraf, M.U.; Terriche, Y.; Niazi, K.A.K.; Su, C.; Vasquez, J.C.; Guerrero, J.M. Battery Energy Storage Systems for Mitigating Fluctuations Caused by Pulse Loads and Propulsion Motors in Shipboard Microgrids. In Proceedings of the 2019 IEEE 28th International Symposium on Industrial Electronics (ISIE), Vancouver, BC, Canada, 12–14 June 2019; pp. 1047–1052.
4. Rocabert, J.; Capo-Mistut, R.; Munoz-Aguilar, R.S.; Candela, J.I.; Rodriguez, P. Control of Energy Storage System Integrating Electrochemical Batteries and Supercapacitors for Grid-Connected Applications. *IEEE Trans. Ind. Appl.* **2019**, *55*, 1853–1862. [[CrossRef](#)]
5. Ravada, B.R.; Tummuru, N.R. Control of a Supercapacitor-Battery-PV Based Stand-Alone DC-Microgrid. *IEEE Trans. Energy Convers.* **2020**, *35*, 1268–1277. [[CrossRef](#)]
6. Chen, X.; Shi, M.; Zhou, J.; Chen, Y.; Zou, W.; Wen, J.; He, H. Distributed Cooperative Control of Multiple Hybrid Energy Storage Systems in a DC Microgrid Using Consensus Protocol. *IEEE Trans. Ind. Electron.* **2020**, *67*, 1968–1979. [[CrossRef](#)]
7. Xie, W.; Han, M.; Cao, W.; Guerrero, J.M.; Vasquez, J.C. System-Level Large-Signal Stability Analysis of Droop-Controlled DC Microgrids. *IEEE Trans. Power Electron.* **2021**, *36*, 4224–4236. [[CrossRef](#)]
8. Marx, D.; Magne, P.; Nahid-Mobarakeh, B.; Pierfederici, S.; Davat, B. Large Signal Stability Analysis Tools in DC Power Systems with Constant Power Loads and Variable Power Loads—A Review. *IEEE Trans. Power Electron.* **2012**, *27*, 1773–1787. [[CrossRef](#)]
9. Wan, C.; Qian, W.; Zhao, C.; Song, Y.; Yang, G. Probabilistic Forecasting Based Sizing and Control of Hybrid Energy Storage for Wind Power Smoothing. *IEEE Trans. Sustain. Energy* **2021**, *2*, 1841–1852. [[CrossRef](#)]
10. Xu, H.; Liu, Y.; Dong, G.; Sun, X. Stability Analysis and Compensation Methods to Improve Stability for DC Microgrid with Constant Power Loads. In Proceedings of the 2021 IEEE 4th International Electrical and Energy Conference (CIEEC), Wuhan, China, 26–29 March 2021; pp. 1–7.
11. Wang, B.; Wang, Y.; Xu, Y.; Zhang, X.; Gooi, H.B.; Ukil, A.; Tan, X. Consensus-Based Control of Hybrid Energy Storage System With a Cascaded Multiport Converter in DC Microgrids. *IEEE Trans. Sustain. Energy* **2020**, *11*, 2356–2366. [[CrossRef](#)]
12. Lee, N.; Nee, C.H.; Yap, S.S.; Tham, K.K.; You, A.H.; Yap, S.L.; Arof, A.K.B. Capacity Sizing of Embedded Control Battery–Supercapacitor Hybrid Energy Storage System. *Energies* **2022**, *15*, 3783. [[CrossRef](#)]
13. Baboo, J.P.; Jakubczyk, E.; Yattoo, M.A.; Phillips, M.; Grabe, S.; Dent, M.; Hinder, S.J.; Watts, J.F.; Lekakou, C. Investigating battery-supercapacitor material hybrid configurations in energy storage device cycling at 0.1 to 10C rate. *Power Sources* **2023**, *561*, 232762. [[CrossRef](#)]
14. Zhang, X.; Wang, B.; Gamage, D.; Ukil, A. Model Predictive Control Based Dynamic Power Loss Prediction for Hybrid Energy Storage System in DC Microgrids. *IEEE Trans. Ind. Electron.* **2022**, *69*, 8080–8090. [[CrossRef](#)]
15. Vafamand, N.; Yousefifzadeh, S.; Khooban, M.H.; Bendtsen, J.D.; Dragicevic, T. Adaptive TS Fuzzy-Based MPC for DC Microgrids With Dynamic CPLs: Nonlinear Power Observer Approach. *IEEE Syst. J.* **2019**, *13*, 3203–3210. [[CrossRef](#)]
16. Liu, S.; Zheng, J.; Li, R.; Li, X.; Fang, W.; Liu, X. Multiple Lyapunov Function-Based Large Signal Stability Analysis of DC Microgrid with Coordinated Control. In Proceedings of the 2019 22nd International Conference on Electrical Machines and Systems (ICEMS), Harbin, China, 11–14 August 2019; pp. 1–6.
17. Kaban, M.; Singh, P.; Niebur, D. A Design and Optimization Tool for Inverter-Based Microgrids Using Large-Signal Nonlinear Analysis. *IEEE Trans. Smart Grid* **2019**, *10*, 4566–4576. [[CrossRef](#)]
18. Wu, J.; Lu, Y. Adaptive Backstepping Sliding Mode Control for Boost Converter with Constant Power Load. *IEEE Access* **2019**, *7*, 50797–50807. [[CrossRef](#)]
19. Abadi, S.A.G.K.; Habibi, S.I.; Khalili, T.; Bidram, A. A Model Predictive Control Strategy for Performance Improvement of Hybrid Energy Storage Systems in DC Microgrids. *IEEE Access* **2022**, *10*, 25400–25421. [[CrossRef](#)]
20. Zhong, Z.X. Tracking synchronization for DC microgrid with multiple-photovoltaic arrays: An even-based fuzzy control scheme. *IEEE Access* **2018**, *6*, 24996–25006. [[CrossRef](#)]

21. Goh, H.H.; Kang, J.; Zhang, D.; Liu, H.; Dai, W.; Kurniawan, T.A.; Goh, K.C. Improve the performance of DC microgrids by utilizing adaptive Takagi-Sugeno (TS) model predictive control (MPC). *CSEE J. Power Energy Syst.* **2022**, *9*, 1472–1481.
22. Liu, S.; Li, X.; Xia, M.; Qin, Q.; Liu, X. Takagi-Sugeno Multimodeling-Based Large Signal Stability Analysis of DC Microgrid Clusters. *IEEE Trans. Power Electron.* **2021**, *36*, 12670–12684. [[CrossRef](#)]
23. Kabalan, M.; Singh, P.; Niebur, D. Large Signal Lyapunov-Based Stability Studies in Microgrids: A Review. *IEEE Trans. Smart Grid* **2017**, *8*, 2287–2295. [[CrossRef](#)]
24. Wu, F.; Lian, J. Stabilization of constrained switched systems via multiple Lyapunov R-functions. *Syst. Control. Lett.* **2020**, *139*, 104686. [[CrossRef](#)]
25. Chang, F.; Cui, X.; Wang, M.; Su, W.; Huang, A. Large-Signal Stability Criteria in DC Power Grids with Distributed-Controlled Converters and Constant Power Loads. *IEEE Trans. Smart Grid* **2020**, *11*, 5273–5287. [[CrossRef](#)]
26. Starke, M.; Bhowmik, P.; Xiao, B.; Moorthy, R.S.K.; Campbell, S.; Dean, B.; Thapa, A.; Chinthavali, M. Secondary Use-Plug-and-Play Energy Storage System Composed of Multiple Energy Storage Technologies. In Proceedings of the 2021 IEEE Power & Energy Society Innovative Smart Grid Technologies Conference (ISGT), Washington, DC, USA, 16–18 February 2021; pp. 1–5.
27. Liu, X.; Zhou, Y.; Zhang, W. Stability criteria for constant power loads with multistage LCL filters. *IEEE Trans. Veh. Technol.* **2011**, *60*, 2042–2049. [[CrossRef](#)]
28. Chang, F.; Cui, X.; Wang, M.; Su, W. Potential-Based Large-Signal Stability Analysis in DC Power Grids With Multiple Constant Power Loads. *IEEE Open Access J. Power Energy* **2022**, *9*, 16–28. [[CrossRef](#)]
29. Peng, D.; Huang, M.; Li, J.; Sun, J.; Zha, X.; Wang, C. Large-Signal Stability Criterion for Parallel-Connected DC–DC Converters With Current Source Equivalence. *IEEE Trans. Circuits Syst. II Express Briefs* **2019**, *66*, 2037–2041. [[CrossRef](#)]
30. Lin, P.; Zhang, C.; Wang, J.; Jin, C.; Wang, P. On Autonomous Large-Signal Stabilization for Islanded Multibus DC Microgrids: A Uniform Nonsmooth Control Scheme. *IEEE Trans. Ind. Electron.* **2020**, *67*, 4600–4612. [[CrossRef](#)]
31. Xu, Q.; Jiang, W.; Blaabjerg, F.; Zhang, C.; Zhang, X.; Fernando, T. Backstepping Control for Large Signal Stability of High Boost Ratio Interleaved Converter Interfaced DC Microgrids with Constant Power Loads. *IEEE Trans. Power Electron.* **2020**, *35*, 5397–5407. [[CrossRef](#)]
32. Jiang, J.; Liu, F.; Pan, S.; Zha, X.; Liu, W.; Chen, C.; Hao, L. A Conservatism-Free Large Signal Stability Analysis Method for DC Microgrid Based on Mixed Potential Theory. *IEEE Trans. Power Electron.* **2019**, *34*, 11342–11351. [[CrossRef](#)]
33. Liu, X.; Sun, X. Large Signal Stability analysis of Hybrid AC/DC microgrid Based on T-S fuzzy model method. In Proceedings of the 2019 22nd International Conference on Electrical Machines and Systems (ICEMS), Harbin, China, 11–14 August 2019; pp. 1–6.
34. Ming, J.; Wang, Y.; Wang, F.; Su, B. Large-Signal Stability Analysis and Shunt Active Damper Compensation for DC Microgrid with Multiple Constant Power Loads. In Proceedings of the 2019 22nd International Conference on Electrical Machines and Systems (ICEMS), Harbin, China, 11–14 August 2019; pp. 84–89.
35. Liu, Z.; Ge, X.; Su, M.; Han, H.; Xiong, W.; Gui, Y. Complete Large-Signal Stability Analysis of DC Distribution Network via Brayton-Moser’s Mixed Potential Theory. *IEEE Trans. Smart Grid* **2023**, *14*, 866–877. [[CrossRef](#)]
36. Gui, Y.; Han, R.; Guerrero, J.; Vasquez, J.; Wei, B.; Kim, W. Large-Signal Stability Improvement of DC-DC Converters in DC Microgrid. *IEEE Trans. Energy Convers.* **2021**, *36*, 2534–2544. [[CrossRef](#)]
37. Li, Z.; Kong, L.; Pei, W.; Ye, H.; Deng, W. Large-Disturbance Stability Analysis of Droop-Controlled DC Microgrid Based on Mixed Potential Function. *Power Syst. Technol.* **2018**, *42*, 3725–3734.

Disclaimer/Publisher’s Note: The statements, opinions and data contained in all publications are solely those of the individual author(s) and contributor(s) and not of MDPI and/or the editor(s). MDPI and/or the editor(s) disclaim responsibility for any injury to people or property resulting from any ideas, methods, instructions or products referred to in the content.